Identification of distinct ChAT+ neurons and activity-dependent control of postnatal SVZ neurogenesis

Patricia Paez-Gonzalez[1,7], **Brent Asrican**[1,7], **Erica Rodriguez**[2,7], and **Chay T. Kuo**[1,2,3,4,5,6,*]

[1]Department of Cell Biology, Duke University School of Medicine, Durham, NC 27710, USA

[2]Neurobiology Graduate Training Program, Duke University School of Medicine, Durham, NC 27710, USA

[3]Brumley Neonatal Perinatal Research Institute, Department of Pediatrics, Duke University School of Medicine, Durham, NC 27710, USA

[4]Department of Neurobiology, Duke University School of Medicine, Durham, NC 27710, USA

[5]Preston Robert Tisch Brain Tumor Center, Duke University School of Medicine, Durham, NC 27710, USA

[6]Duke Institute for Brain Sciences, Duke University School of Medicine, Durham, NC 27710, USA

Abstract

Postnatal/adult SVZ neurogenesis is believed to be primarily controlled by neural stem cell (NSC)-intrinsic mechanisms, interacting with extracellular/niche-driven cues. Although behavioral paradigms and disease states have suggested possibilities for higher-level inputs, it is currently unknown if neural activity patterns from discrete circuits can directly regulate SVZ neurogenesis. We have identified a previously undescribed population of ChAT+ neurons residing within the rodent SVZ neurogenic niche. These neurons showed morphological and functional differences from neighboring striatal counterparts, and released acetylcholine locally in activity-dependent fashion. Optogenetic inhibition and stimulation of subependymal ChAT+ neurons in vivo showed that they are necessary and sufficient to control neurogenic proliferation. Furthermore, whole-cell recordings and biochemical experiments revealed direct SVZ NSC responses to local acetylcholine release, synergizing with FGF receptor activation to increase neuroblast production. These results uncovered an unknown gateway connecting SVZ neurogenesis to neuronal activity-

*Correspondence should be addressed to C.T.K. (chay.kuo@duke.edu).
[7]These authors contributed equally to this work.

Author Contributions

P.P.-G. designed, performed anatomical, IHC staining, and biochemical experiments; B.A., P.P.-G. designed, performed in vivo optogenetic experiments; B.A., E.R., C.T.K. designed, performed electrophysiological recordings; B.A, C.T.K. designed, performed imaging experiments; C.T.K. conceived the project. P.P.-G., B.A., E.R. assembled figures; P.P.-G., B.A., C.T.K. wrote the paper. All authors discussed results and commented on the manuscript.

Competing Financial Interests

The authors declare no competing financial interests.

A supplementary methods checklist is available.

dependent control, and possibilities for modulating neuroregenerative capacities in health and disease.

INTRODUCTION

Robust generation of adult born neurons, from the rodent subventricular/subependymal zone (SVZ/SEZ) neurogenic niche, is a useful experimental system for studying regenerative capacities in the mammalian brain. SVZ neurogenesis provides tractable assays to tackle molecular and cellular-level mechanisms regulating addition of new neurons into established neural circuits[1–3]. It also serves as a wonderful model for understanding how tissue stem cells and their progeny respond to injury and disease[4–6]. The consensus view currently is that postnatal/adult SVZ neurogenesis is mediated by subependymal GFAP$^+$ B-type astrocytes functioning as neural stem cells (NSCs), producing transiently amplifying Mash1$^+$ progenitors that differentiate into DCX$^+$ neuroblasts, which then migrate to the olfactory bulb through the rostral migratory stream. While the term "SVZ neurogenesis" is widely used to describe this process, neuroblasts are born in the subependymal space around the lateral brain ventricles.

As in other tissue stem cell niches, self-renewal of SVZ NSCs and production of differentiating progeny are controlled by well-conserved cell-intrinsic molecular pathways[7,8]. In addition, extracellular factors and cell-cell interactions within the NSC microenvironment also play critical roles. For example, blood vessels within the SVZ niche have been shown to regulate NSC function by acting as sources for neurogenic signals[9,10]. And ependymal cells lining the ventricular surface can provide instructive cues to sustain new neuron production, as well as redirecting NSC responses to local tissue damage[11,12]. Together, the SVZ niche provides a rich environment for trophic factors, coordinating NSC homeostasis[13,2].

Other than classical stem cell niche factors, neurotransmitters, common currencies for neural circuit activity and modulation, have also been shown to play important roles during adult SVZ neurogenesis[14,15]. Excitatory neurotransmitter glutamate can influence proliferation and differentiation of neural progenitors through mGluR activation[16,17]. Glutamate also enhances survival of DCX$^+$ neuroblasts and newborn neurons through activating NMDA receptors[18,17]. Meanwhile, inhibitory neurotransmitter GABA is believed to control progenitor proliferation through GABA$_A$ receptor[19,20], activating voltage-gated calcium channels in SVZ astrocytes[21]. Modulatory neurotransmitter dopamine has also been shown to stimulate SVZ proliferation[22] through increased EGF secretion[23]. Serotonin[24,25], as well as cholinergic activation[26,27] are believed to have similarly positive effects on SVZ cellular proliferation. Despite this knowledge, it remains unclear whether neuronal activity can directly regulate postnatal/adult SVZ neurogenesis, as the exact neurons capable of performing such functions have not been identified. It is currently unknown if the SVZ niche contains resident neurons that provide local innervation.

We performed a direct comparison of neurotransmitters in vitro for their neurogenic properties. There we found that acetylcholine (ACh) has a profound effect in increasing DCX$^+$ neuroblast production. In search for potential ACh sources in vivo, we uncovered a

previously undescribed population of ChAT^{+} neurons residing within and innervating the SVZ niche, with distinct morphological/functional properties from cholinergic neurons in the neighboring striatum. Identification of these subependymal ChAT^{+} neurons and our experiments to determine their functions revealed an important gateway connecting postnatal/adult SVZ neurogenesis to neuronal activity-dependent modulation.

RESULTS

Neurotransmitter effect on neuroblast production in vitro

We reasoned that defining neurotransmitters with potent neurogenic capabilities may reveal the exact neurons directly controlling SVZ neurogenesis. Starting with the SVZ NSC adherent culture assay, we compared several key neurotransmitters on their abilities to enhance DCX[+] neuroblast production. We differentiated passage two SVZ adherent cultures in the presence of select concentrations of neurotransmitters, focusing particularly on glutamate, GABA, serotonin, dopamine, and acetylcholine (Supplementary Fig. 1a). We scored the effects of these neurotransmitters on neuroblast production after 5 days of in vitro differentiation by making protein lysates from individually treated culture plate wells, and performed Western blotting analyses on DCX protein levels (Supplementary Fig. 1b). This revealed a potent neurogenic effect of modulatory neurotransmitter ACh on the production of DCX[+] neuroblasts from differentiating SVZ NSC cultures (Supplementary Fig. 1a,b), which was sensitive to nicotinic or muscarinic inhibition (Supplementary Fig. 1c).

Genetic disruption of cholinergic circuit activity

Due to the overall physiological importance of ACh, genetic deletions of ChAT[28], or the vesicular acetylcholine transporter[29], resulted in similar lethal phenotypes shortly after birth. It had been shown previously that disruption of Ankyrin 3 (Ank3 or AnkyrinG), a large adapter protein necessary for proper axonal initial segment assembly and function, in cerebellar Purkinje neurons resulted in significant defects in their abilities to initiate action potentials[30]. To adopt a similar strategy we generated a conditional floxed-allele for the *ank3* locus (Supplementary Fig. 2a). We crossed *ank3*[flox/+] mice to β-*actin-Cre* driver to generate *ank3*[KO/+] mice, which upon intercross produced *ank3*[KO/KO] mutants. These mutant animals died shortly after birth. Protein extracts made from whole-brain lysates confirmed a protein-null mutation for the 480 and 270 kD isoforms of Ank3 (Supplementary Fig. 2b), expressed by wild-type ChAT^{+} neurons (Supplementary Fig. 2b), which are known to localize to axon initial segments[31].

To conditionally remove Ank3 from cholinergic neurons, we crossed *ChAT*[IRES-Cre/+]; *ank3*[flox/+] mice to *ank3*[flox/+]; *R26R-tdTomato*[flox/flox] stocks to generate *ChAT*[IRES-Cre/+]; *ank3*^{+/+}; *R26R-tdTomato*[flox/+] (control), *ChAT*[IRES-Cre/+]; *ank3*[flox/+]; *R26R-tdTomato*[flox/+] (Het), and *ChAT*[IRES-Cre/+]; *ank3*[flox/flox]; *R26R-tdTomato*[flox/+] (cKO) animals. The presence of Cre-dependent tdTomato reporter allowed us to visualize ChAT^{+} neurons for functional studies. Ank3-cKO animals were born in Mendelian ratio and showed no evidence of perinatal lethality (32 of 232 animals genotyped at P7 were cKO mutants, 13.8% compared to expected 12.5%). We observed occasional shaking in the movements of cKO animals but otherwise did not detect obvious phenotypic defects. IHC staining of tdTomato[+] cholinergic

neurons from cKO mice showed the lack of Ank3 signal in their proximal axonal segments (Supplementary Fig. 2c). Similar to what had been observed in Purkinje neurons[30], cholinergic neurons from the striatum of cKO mice showed noticeable defects in action potential generation to stimuli, with increasing defects to stronger inputs (Supplementary Fig. 2d). Interestingly, we also detected defects in Ank3-Het ChAT^{+} neurons, and this is likely due to differences in Ank3 expression, since *ank3*[KO/+] heterozygous mice showed lower overall Ank3 protein levels in the brain as compared to wild-type littermates (Supplementary Fig. 2b). These functional defects are consistent with the notion that cholinergic neurons in cKO mice are unable to effectively relay inputs into action potentials, and subsequent release of ACh.

When we examined DCX[+] neuroblast production in these Ank3-cKO animals, we saw a marked reduction in neuroblast chains along the ventricular wall (Fig. 1a). This defect in SVZ neurogenesis was noticeable at P14, becoming severe at P30 (Fig. 1b–c; % DCX[+] IHC staining coverage/ventricular area: Ctrl = 11.71 ± 0.98, cKO = 4.09 ± 0.83 (mean ± s.e.m.); $n = 5$; $P < 0.01$, $z = 2.611$, Wilcoxon two-sample test). Ki67 IHC staining showed a corresponding decrease in SVZ cell proliferation in these animals (Fig. 1d,e), while caspase 3 staining showed no obvious increase in cellular apoptosis (data not shown). Consistent with this decrease in SVZ neuroblasts, we observed diminished Mash1^{+} transiently amplifying progenitors within the SVZ niche of P30 Ank3-cKO mice as compared to controls (Fig. 1d,e).

ACh exerts its function locally as it is rapidly degraded by extracellular acetylcholinesterases. Since striatal cholinergic neurons are anatomically adjacent to the SVZ niche, to understand whether their ACh release could be an important contributor to sustaining robustness of SVZ DCX[+] neuroblast production, we analyzed a genetic mouse model where ACh release from striatal cholinergic neurons was largely eliminated[32]. We performed IHC staining for DCX, Ki67, and Mash1 and found no obvious SVZ neurogenesis defects in P30 *Nkx2.1-Cre; ChAT*[flox/flox] mutant mice vs. *Nkx2.1-Cre; ChAT*[flox/+] littermate controls (Supplementary Fig. 3).

Identification of subependymal ChAT^{+} neurons

We next set out to investigate potential sources for ACh within the SVZ neurogenic niche. To determine if the SVZ received direct cholinergic innervation, immunohistochemical (IHC) staining of SVZ whole-mounts with anti-ChAT antibody showed extensive ChAT[+] processes within the niche (Fig. 2a). 3D reconstruction of these ChAT[+] processes showed that they reside in close proximity to the subependymal space (Fig. 2a). We did not detect ChAT expression in SVZ ependymal niche cells, or B-type astrocytes and their progeny in the niche (data not shown). To determine if these ChAT[+] SVZ processes may be from ChAT^{+} cholinergic neurons, we performed IHC antibody staining on SVZ whole-mounts from *ChAT*[IRES-Cre/+]*; Rosa26R-tdTomato (R26R-tdTomato)* transgenic mice, which utilizes Cre expression in ChAT^{+} neurons and Rosa26 Cre-dependent reporter to genetically express tdTomato. They showed that tdTomato[+] processes in the SVZ co-labeled with ChAT, as well as vesicular acetylcholine transporter (VAChT) specific antibodies (Supplementary Fig. 4a).

We noticed large ChAT[+] neuronal cell bodies residing within the SVZ niche in the subependymal space (Fig. 2a,b). DiI-filling of these subependymal ChAT[+] (subep-ChAT^{+}) neurons, visualized via *ChAT-EGFP* mice, showed that they have complex arborization of neuronal processes (Fig. 2c). Using Ank3 IHC co-staining of axon initial segments to distinguish axons from dendrites, we observed that these subep-ChAT^{+} neurons project their axonal processes locally in the subependymal space (Fig. 2c,d and data not shown). Comparing to similarly DiI-filled striatal ChAT^{+} neurons, a noticeable morphological difference was that these subep-ChAT^{+} neurons appear mostly planar, paralleling the ependymal surface above, as compared to the 3D space-filling profile seen in striatal ChAT^{+} neurons (Fig. 2d,e, Supplementary Fig. 4b–d and data not shown). In Ank3-cKO mutant mice, as expected we found defective action potential generation from subep-ChAT^{+} neurons (Fig. 3a–c). When we performed IHC staining against tdTomato in *Nkx2.1-Cre; R26R-tdTomato* mice, we found that unlike their striatal counterparts[32], subep-ChAT^{+} neurons were mainly tdTomato[−] (Fig. 3d), thus not targeted in *Nkx2.1-Cre; ChAT*[flox/flox] mice. *Gsx2-Cre* driver also did not label subep-ChAT^{+} neurons (Fig. 3e). It has been reported that *Drd2-Cre* can target cholinergic neurons in the striatum[33]. We found tdTomato[+] subep-ChAT^{+} neurons in *Drd2-Cre; R26R-tdTomato* mice (Fig. 3e), and *Drd2-Cre; ChAT*[flox/flox] mice showed SVZ neurogenesis defects compared to littermate controls (Fig. 3f–h).

Functional properties of subependymal ChAT^{+} neurons

The morphological and anatomical location differences between subependymal and striatal ChAT^{+} neurons raised the important question of whether they exhibit functional variations. Whole-cell recordings of ChAT^{+} neurons from P28 to P35 *ChAT*[IRES-Cre/+]*; R26R-tdTomato* animals showed that the subependymal population and their striatal counterpart had similar firing rates in response to current injection (Supplementary Fig. 5a). Both neuronal populations showed I_h sag current, but exhibited some differences in membrane electrophysiological properties (Supplementary Fig. 5b,c). In cell-attached recording configuration from similarly prepared acute brain slices, striatal ChAT^{+} neurons showed characteristic patterns of spontaneous activity[34] (Fig. 4a,b; spontaneous firing frequency (Hz) = 1.786 ± 0.266 (mean $\pm$ s.e.m.); $n = 21$). Surprisingly, cell-attached recordings of subep-ChAT^{+} neurons showed little spontaneous activity (Fig. 4c; spontaneous firing frequency (Hz) = 0.042 ± 0.013 (mean $\pm$ s.e.m.); $n = 53$; $P < 0.0001$, $t_{72} = 5.089$; Student's t test). Although they can be evoked to fire action potentials after local release of glutamate via puff pipette (Fig. 4d,e).

To further confirm these differences in evoked vs. spontaneous activities between subependymal and striatal ChAT^{+} neurons, we crossed the *ChAT*[IRES-Cre/+] driver line to *Rosa26R-ChR2EYFP (R26R-ChR2EYFP)* mice to express channelrhodopsin in ChAT^{+} neurons. Repeating the same cell-attached recording experiments, as expected we observed blue light-activated transient pause in spontaneous activity in striatal ChAT^{+} neurons (Fig. 4f), similar to previous observations[35]. Again, subep-ChAT^{+} neurons showed little spontaneous activity, but responded robustly to blue light activation by continuously firing action potentials during the duration of stimulation (Fig. 4g). These results showed that not

only do subependymal and striatal ChAT^{+} neurons differ morphologically, they also exhibit different activity states.

Activity-dependent ACh release in the SVZ niche

ChAT-expressing neurons can synthesize and release ACh. To detect ACh release from subep-ChAT^{+} neurons, we used an ACh sensor: the M1 muscarinic receptor cell-based neurotransmitter fluorescent engineered reporter (M1-CNiFER)[36]. These modified HEK293 cells express Ca^{2+} indicator protein TN-XXL and the M1 muscarinic receptor. ACh binding to M1 receptor results in enhanced fluorescence resonance energy transfer (FRET) between CFP and YFP domains of TN-XXL indicator[36] (Supplementary Fig. 6a). We used 920 nm multiphoton laser excitation, and simultaneously recorded M1-CNiFER fluorescence emissions at 475 nm (CFP) and 530 nm (YFP). ACh application to adherent M1-CNiFER cells resulted in consistent and opposing responses in CFP vs. YFP fluorescence (Fig. 5a), and corresponding fractional changes in FRET ratio (Fig. 5b), consistent with previously published results[36]. To determine whether M1-CNiFER cells can detect ACh release in the SVZ niche, we transplanted them into the subependymal space of SVZ niche in acute brain slice preparations from P30 wild-type mice (Supplementary Fig. 6b). Using the same imaging protocol described above on transplanted M1-CNiFER cells, we detected consistent F/F fluorescence and fractional changes in FRET ratio following ACh application (Fig. 5c).

We next repeated this SVZ transplantation experiment, using acute slices prepared from P30 *ChAT*[IRES-Cre/+]; *R26R-ChR2EYFP* mice. Instead of direct ACh application, we used 473 nm light pulses to locally excite subep-ChAT^{+} neurons and measured M1-CNiFER cell responses (Supplementary Fig. 6c). This resulted in consistent F/F fluorescence and fractional FRET changes in M1-CNiFER cells (Fig. 5d), in agreement with activity-dependent release of ACh from subep-ChAT^{+} neurons. Focal 473 nm light stimulation of ChR2EYFP-expressing striatal ChAT^{+} neurons, either directly adjacent to the SVZ or deeper into the striatum, did not result in measurable SVZ M1-CNiFER cell responses (Fig. 5e). As controls, 473 nm light pulses on M1-CNiFER cells in adherent cultures, or after transplantation into the SVZ of brain slices prepared from non-transgenic mice, showed no F/F fluorescence and FRET changes (data not shown).

SVZ NSCs respond to local ChAT[+] neuron activity

Detection of activity-dependent ACh release led us to look for anatomical relationships between cholinergic processes and the SVZ niche. We performed transmission electron microscopy (TEM) on RFP-antibody stained, immunogold-labeled SVZ samples from *ChAT*[IRES-Cre/+]; *R26R-tdTomato* animals. NSCs in the SVZ niche are identified on TEM through contacts with the brain ventricular surface and their characteristic invaginated nuclei[37]. We detected immunogold-labeled axonal projections from ChAT^{+} neurons, showing intracellular vesicles adjacent to SVZ NSCs (Fig. 6a). Antibody staining against nicotinic and muscarinic receptors revealed their localizations in subependymal GFAP[+] astrocytes near ChAT[+] neuronal processes (Supplementary Fig. 7).

To determine whether SVZ NSCs can directly respond to local ACh release, we prepared acute brain slices from P30 *nestin-CreER^(tm4)*; *R26R-tdTomato; ChAT-ChR2EYFP* mice. P7 tamoxifen injection in these mice resulted in tdTomato expression in SVZ NSCs[6]. We performed whole-cell patch recording on subependymal tdTomato$^+$ NSCs (Supplementary Fig. 8a,b), while focally activating subep-ChAT$^+$ neurons via 473 nm laser, using 10 ms pulses at 15, 30, or 50 Hz for 1 second (Fig. 6b). This resulted in consistent inward currents in SVZ NSCs, which can be blocked by cholinergic receptor antagonists (Fig. 6b–d). Similar results were obtained from subependymal GFP$^+$ type B astrocytes in *GFAP-GFP; ChAT^(IRES-Cre/+); R26R-ChR2EYFP* mice (data not shown). While glutamatergic inhibition did not block this light-induced response in tdTomato$^+$ SVZ NSC, it was TTX-sensitive (Fig. 6b,d). Identical 473 nm light-stimulation experiments performed using brain slices from *nestin-CreER^(tm4); R26R-tdTomato* mice (without *ChAT-ChR2EYFP*) did not induce measurable currents in tdTomato$^+$ SVZ NSCs (Fig. 6b). We did not detect measurable light-induced currents in *nestin-CreER^(tm4); R26R-tdTomato* lineage-traced S100β$^+$ SVZ ependymal niche cells or Mash1$^+$ transiently amplifying progenitors, but did observe light-induced cholinergic currents in DCX$^+$ neuroblasts in the SVZ (Supplementary Fig. 8c–e).

Optogenetic modulation of SVZ cellular proliferation

Since our in vitro data showed that ACh has significant neurogenic effects (Supplementary Fig. 1), to examine whether activation of subep-ChAT$^+$ neurons can result in increased cellular proliferation in vivo, we implanted optical fibers targeting the lateral ventricle of P30 *ChAT^(IRES-Cre/+); R26R-ChR2EYFP* mice (Supplementary Fig. 9a, Fig. 7a,b). Phosphorylated ribosomal protein S6 (p-rpS6) is an activity-dependent gene marker for cholinergic neurons in vivo[38,39]. IHC staining using p-rpS6 antibody showed that subep-ChAT$^+$ neurons have robust p-rpS6 expression under physiological conditions (Fig. 7d). Following a light-train protocol effective for optogenetic activation of cholinergic neurons[40] (Fig. 7a,b), p-rpS6 expression in subep-ChAT$^+$ neurons became enhanced after 48 hours of in vivo 473 nm light-stimulation (Fig. 7d). Concurrently, we observed consistent increases in the numbers of Ki67$^+$ proliferating cells in the SVZ niche as compared to fiber-implanted controls without light (Fig. 7e, Supplementary Fig. 9b). Expressions of Mash1, DCX, and numbers of Nestin$^+$Ki67$^+$ SVZ NSCs were upregulated following 48 hours of light-stimulation vs. no-light controls (Fig. 7e, Supplementary Fig. 9b). Identical 48 hours of light-stimulation, in control mice lacking ChR2 expression in ChAT$^+$ neurons, resulted in no noticeable changes to p-rpS6 expression in subep-ChAT$^+$ neurons (data not shown), or SVZ Ki67$^+$, Mash1$^+$, DCX$^+$, Nestin$^+$Ki67$^+$ cell numbers (Fig. 7e).

Conversely, in P30 *ChAT^(IRES-Cre/+); R26R-ArchaerhodopsinGFP (R26R-ArchGFP)* mice we performed the same optogenetic experiment, using 556 nm laser to silence subep-ChAT$^+$ neurons (Supplementary Fig. 9c, Fig. 7c). This resulted in reduced p-rpS6 expression in subep-ChAT$^+$ neurons (Fig. 7f), and corresponding decreases in the numbers of Ki67$^+$, Mash1$^+$, DCX$^+$, and Nestin$^+$Ki67$^+$ cells in the SVZ niche (Fig. 7g, Supplementary Fig. 9d). While p-rpS6 expression changes were robust in subep-ChAT$^+$ neurons following light-stimulation (Fig. 7d,f), we did not observe concurrent p-rpS6 changes in striatal ChAT$^+$ neurons either adjacent to the SVZ or deeper into the striatum (Supplementary Fig. 9e,f). Similar optogenetic experiments using *ChAT^(IRES-Cre/+); R26R-ChR2EYFP* or

ChAT[IRES-Cre/+]*; R26R-ArchGFP* mice, but with light fibers targeting the striatum instead of SVZ resulted in no obvious changes to SVZ neurogenesis (data not shown). Implantation of optical fiber to target the lateral ventricle represents a form of injury. To understand whether microglial proliferation may be part of observed increases in SVZ Ki67^{+} cells following ChR2-stimulation, Iba1, CD11b, as well as IHC staining for NG2, 48 hrs post fiber implantation, found no significant differences in their cell numbers or proliferation comparing light-stimulation vs. no light controls (Supplementary Fig. 10a,b). Consistent with our previous findings[6], we detected a delayed onset of Thbs4 protein induction in the SVZ niche 3+ days after fiber placement (Supplementary Fig. 10c). Since the cascade of injury responses in vivo is complex, we limited our optogenetic analyses to the first 48 hours after fiber placement, prior to significant Thbs4 protein upregulation.

ACh enhances SVZ neurogenesis through the FGFR pathway

It had been reported previously that embryonic cortical progenitors proliferate to ACh stimulation through fibroblast growth factor receptor (FGFR) signaling[41]. Upon FGF ligand binding, FGFR is known to activate via receptor phosphorylation on tyrosine653/654[42]. Following removal of growth factors from primary SVZ NSC culturing media, we detected similar effects on FGFR tyrosine653/654 phosphorylation in SVZ cultures after re-introduction of FGF (Supplementary Fig. 11a, comparing lanes 6 & 9). Addition of ACh alone without FGF resulted in similar increase in FGFR phosphorylation (Supplementary Fig. 11a, lanes 1–3 & 9). To determine if this increase in ACh-mediated FGFR phosphorylation is a direct effect downstream of ACh signal transduction, or an indirect pathway perhaps through increased FGF ligand production, we performed similar experiments as above with shorter incubation periods. Although we can detect FGF-mediated FGFR activation and phosphorylation 90 minutes after FGF addition to media, in the same time course we did not observe noticeable increase in FGFR phosphorylation after ACh addition (Supplementary Fig. 11b), making it less likely that ACh-mediated intracellular signals can directly activate FGFR.

To test whether this delayed increase in ACh-mediated FGFR phosphorylation may in part be secondary to upregulation of FGF production, we used an anti-FGF antibody to block FGF ligand binding to its receptor (Supplementary Fig. 11a, lanes 6–8). Whereas addition of ACh alone resulted in increased FGFR phosphorylation (Supplementary Fig. 11a, lanes 1–3, 9), concurrent incubation with anti-FGF antibody blunted this increase (Supplementary Fig. 11a, lanes 4, 5). ELISA assay to detect presence of FGF in the culture media during in vitro differentiation showed corresponding FGF increases in the ACh-treated conditions compared to controls (Supplementary Fig. 11c). In similar experiments we did not detect epidermal growth factor receptor (EGFR) activation following ACh addition to SVZ NSC cultures (Supplementary Fig. 11d). Furthermore, anti-FGF antibody co-incubation also blunted ACh-induced DCX[+] neuroblast production in culture (Supplementary Fig. 11e), consistent with the notion that local release of ACh in the SVZ niche in an activity-dependent manner induces NSC production of new neuroblasts. This idea is further supported by decreased levels of phospho-FGFR staining in subependymal GFAP[+] NSCs in P30 Ank3-cKO mice compared to littermate controls (Supplementary Fig. 11f).

DISCUSSION

Starting with an in vitro assay to identify neurogenic neurotransmitters, we found that ACh has a potent effect on DCX[+] neuroblast production from postnatal SVZ NSCs. In search of potential sources for ACh in the SVZ niche, we uncovered direct cholinergic inputs from local subep-ChAT^{+} neurons. This previously undescribed subpopulation of cholinergic neurons showed morphological and functional differences from their neighboring striatal counterpart, and can release ACh into the niche in activity-dependent fashion. In vivo optogenetic manipulation of subep-ChAT^{+} neurons revealed that their activity is both necessary and sufficient to modulate SVZ neurogenic proliferation. Lastly, we demonstrated that SVZ NSCs can respond to ACh release, which then function through FGFR signaling pathway to increase neuroblast production. These results will have important implications for understanding circuit-level control of postnatal/adult SVZ neurogenesis in health and disease.

Cholinergic circuit control of SVZ neurogenesis

The systemic importance of ACh is perhaps best demonstrated by early postnatal lethality of animals lacking either ChAT[28], or VAChT[29]. ACh can be released via both bulk (non-vesicular) and vesicular (neuronal activity dependent) mechanisms. Together they modulate wide-ranging cellular and neural circuit-level functions such as neuromuscular control, and striatal gating of cortical vs. thalamic inputs[35]. Cholinergic signaling has also been reported to influence rodent SVZ neurogenesis: in vivo infusion of nicotinic agonist can result in increased SVZ cellular proliferation as measured by BrdU incorporation[27]. Since the endogenous sources for ACh mediating these effects were unknown, it remained possible that indirect actions of cholinergic pharmacology may be responsible for observed phenotype.

To genetically test the importance of cholinergic circuitry on SVZ neurogenesis, and to overcome early lethality associated with ChAT and VAChT deletions, we took an approach to blunt cholinergic neurons' ability to properly scale action potential generation to strengths of stimuli. This enabled us to demonstrate that cholinergic neurons' ability to fire precise action potentials is important to maintain robustness of adult SVZ neurogenesis. As a neurotransmitter, ACh exerts its function locally due to rapid degradation by extracellular acetylcholinesterases. Since striatal ChAT^{+} neurons are anatomically adjacent to the SVZ niche, we analyzed a genetic mouse model where ACh from striatal ChAT^{+} neurons was largely eliminated[32], but detected no obvious SVZ neurogenesis defects.

Our discovery that the SVZ niche is directly innervated by local subep-ChAT^{+} neurons points to exciting future directions for understanding circuit-level control of new neuron production. Subep-ChAT^{+} neurons highly expressed the neuronal activity-dependent marker p-rpS6[39], indicating that these neurons are normally active in vivo. However, they do not spontaneously fire action potentials in acute slice preparations. Since spontaneous firing of striatal cholinergic neurons is generated by intrinsic membrane properties instead of synaptic drive[34], it is possible that membrane property differences contribute to the lack of spontaneous activity in subep-ChAT^{+} neurons. It is also possible that the functional connectivity for subep-ChAT^{+} neurons differs from striatal counterparts, though potential

sources for excitatory/inhibitory inputs are currently unknown and will require circuit-tracing strategies to identify. Functional experiments have suggested that the rates of adult SVZ neurogenesis can be influenced by pregnancy[43,44], male pheromone preference during mating[45], as well as paternal recognition of offspring[46]. While it is currently unclear whether subep-ChAT+ neuron activity patterns can be influenced by these behavioral paradigms, known neural circuits involved in mediating these behaviors may serve as entry points into understanding connectivity of subep-ChAT+ neurons.

NSC proliferation and neuroblast production

Throughout embryonic and postnatal development NSCs self-renew and generate progeny through cell-intrinsic mechanisms interacting with microenvironmental cues. Recent results from adult hippocampal neurogenesis showed that local neural circuits can play important roles in NSC proliferation and differentiation[47–49]. This emerging view on connections between neural circuits and stem cell biology is exciting as it can be an elegant way to tie together external inputs, circuit-level coding, and NSC fate choices to make lasting structural changes via new neuron production. SVZ NSCs require an array of growth factors to sustain self-renewal and balance proliferation/differentiation: EGF is perhaps one of the best studied, and is a key ingredient for successful culturing of NSCs ex vivo since it promotes NSC proliferation. Another important growth factor for SVZ NSCs is FGF. Here we showed that ACh preferentially synergizes with FGFR but not EGFR activation, which begin to suggest cellular mechanisms for how neural modulation may feed into canonical stem cell regulatory loops.

The inhibitory neurotransmitter GABA has been shown to enhance maturation of newborn SVZ neuroblasts[50]. Though GABA's important function on neuronal inhibition is not "lost" on this system, as its increased level feed back on NSCs to dampen their proliferation[19,20]. This elegant parallel usage of neurotransmitter for neural circuit and NSC control may ensure efficient integration of these two biological processes in the brain. Future experiments aimed to address intersections between neurotransmitters and known pathways controlling NSC proliferation/differentiation should shed further light on our understanding of circuit-level control of neurogenesis.

METHODS

Animals

All mouse experiments were performed according to an approved protocol by the Institutional Animal Care and Use Committee at Duke University. The following mouse lines were purchased from JAX: *ChAT*IRES-Cre/+ (#006410); *ChAT*flox/+ (#016920); *Nkx2.1-Cre* (#008661); *R26R-ChR2EYFP* (#012569); *R26R-ArchGFP* (#012735); *ChAT-ChR2EYFP* (#014545); *GFAP-GFP* (#003257). *Drd2-Cre*[51] and *ChAT-EGFP*[52] mice were purchased from MMRRC. Generation of *ank3* mutant allele was as described[53].

Cell culture, imaging, and analyses

Adherent SVZ NSC culture and differentiation were performed as described[54]. ACh, dopamine, muscimol, serotonin, glutamate, mecamylamine, atropine (Tocris), bFGF and

EGF (Invitrogen), and α-FGF neutralizing Ig[55] (mouse, Millipore) were used at concentrations as described for each experiment, and added fresh daily during in vitro differentiation. For FGF ELISA assay, SVZ culture was differentiated in 2 ml media, and 100 μl was collected for analysis at times indicated following manufacturer's protocol (FGF mouse ELISA kit, Abcam). In vivo tamoxifen induction was performed as described[11]. All IHC staining images were acquired on Leica TCS SP5 confocal microscope, with control and experimental samples imaged under identical instrument settings. Imaris software was used for 3D image projections, signal co-localization, and quantifications as described[12]. Counting of SVZ proliferating cells was performed as described[56].

Immunohistochemical staining and electron microscopy

Preparation of brain tissue for immunohistochemistry (IHC) was as described[11,57]. Primary antibodies against the following antigens were used: GFP (#GFP-1020, 1:500, Aves Labs); RFP (#600-401-379, 1:1000, Rockland); ChAT (#AB144P, 1:100, Millipore); VAChT (#G4481, 1:100, Promega); DCX (#AB2253, 1:200, Millipore); Phospho-S6 Ribosomal Protein (#2215, 1:200, Cell Signaling); Ki67 (#ab15580, 1:800, Abcam); Mash1 (#556604, 1:100, BD Pharmigen); Nestin (#Rat-401, 1:50, Dev. Studies Hybridoma Bank); S100β (#SAB1402349, 1:200, Sigma); Iba1(#ab15690, 1:200, Abcam); CD11b (#MCA711G, 1:200, AbD Serotec); NG2 (#MAB6689, 1:200, R&D Systems); Caspase 3 (#9664, 1:200, Cell Signaling); Thbs4 (#AF2390, 1:200, R&D Systems); α3-NicotinicR (#NBP1-87534, 1:400, Sigma); α4-NicotinicR (#AB5590, 1:500, Millipore); MuscarinicR (#10-217, 1:500, Argene); GFAP (#G3893, 1:1000, Sigma); Phospho-FGFR (#3476, 1:500, Cell Signaling). All antibodies used were validated in our previous publications[11,12,6] or by publications available on vendor website specific to each antibody. For Phospho-FGFR staining, samples were blocked/stained in PBST, washed in PBS. For immunogold EM, animals were perfused with 1% glutaraldehyde + 4% paraformaldehyde (Polysciences) in 0.1 M PB according to online protocol (http://synapses.clm.utexas.edu/lab/howto/protocols/Perfusion_Harris_v20090413.pdf). 50 μm vibratome sections were incubated 30 min RT in 1% sodium borohydride (EMS), followed by 1 h RT blocking in 1% BSA, and incubation in primary Ig against RFP ((#600-401-379, 1:1000, Rockland) for 48 h at 4°C. Ultra Small Immunogold (0.8 nm)-conjugated secondary Ig incubation (rabbit, 1:50, EMS) was performed in 0.8% BSA + 0.1% Fish gelatin (CWFS gelatin, Aurion) buffer, 3 h at RT. Gold particles were enhanced using Silver IntenSE kit (Amersham GE) for 12 min, followed by incubation in 2% osmium and dehydrated in a graded % of acetone solutions, all at RT, followed by epoxy mounting. Thin sections were stained using uranyl acetate (EMS) and Reynold's lead citrate (EMS).

Cell-attached and whole-cell electrophysiology

Animals were anesthetized with isofluorane, trans-cardially perfused and then ventricular wall and striatal sections dissected as whole-mounts in ice-cold NMDG-ACSF (containing the following in mM: 92 NMDG, 2.5 KCl, 1.2 NaH_2PO_4, 30 $NaHCO_3$ 20 HEPES, 2 glucose, 5 sodium ascorbate, 2 thiourea, 3 sodium pyruvate, 10 $MgSO_4$, 0.5 $CaCl_2$), and bubbled with 5% CO_2/95% O_2. Tissues were then bubbled in same solution at 37°C for 8 min, transferred to bubbled, modified-HEPES ACSF at RT (containing the following in mM: 92 NaCl, 2.5 KCl, 1.2 NaH_2PO_4, 30 $NaHCO_3$, 20 HEPES, 2 glucose, 5 sodium

ascorbate, 2 thiourea, 3 sodium pyruvate, 2 $MgSO_4$, 2 $CaCl_2$) for at least 1 h before recording. Recordings were performed in submerged chamber, superfused with continuously bubbled ACSF (containing in mM: 125 NaCl, 2.5 KCl, 1.25 NaH_2PO_4, 26 $NaHCO_3$, 20 glucose, 2 $CaCl_2$, 1.3 $MgCl_2$) at 2–5 ml/min at RT. Cell-attached recordings were performed using ACSF-filled micropipettes (4–6 MΩ). Signals were amplified with Multiclamp 700B (filtered at 2 kHz), digitized with Digidata 1440A (5 kHz), recorded using pClamp 10 software (Axon). Internal solutions for whole-cell recordings contained the following in mM: 130 K-gluconate, 2 NaCl, 4 $MgCl_2$, 20 HEPES, 4 Na_2ATP, 0.4 NaGTP, 0.5 EGTA, and Alexa 488 dye (Invitrogen) to visualize patched cells. Signals were amplified with Multiclamp 700B (filtered at 10 kHz), digitized with Digidata 1440A (20 kHz), recorded using pClamp 10. Pipette puff application was performed via TTL control of Picospritzer III (Parker). Light-activation of channelrhodopsin was delivered by TTL control of 473 nm laser (IkeCool). Tracings were analyzed using Neuromatic package (Think Random) in Igor Pro software (WaveMetrics). Voltage threshold for action potential generation was identified as point of most rapid change in membrane potential, determined by analyzing first and second derivatives in current-clamped whole-cell recordings. Average spike shape was generated via aligning traces to peak of 1st action potential after current injection. Time zero = mean time at current pulse initiation.

DiI and DiO-labeling

DiI-labeling was performed according to previously described methods[58] with following modifications: following dissection, samples were fixed for 1 hr at RT with 4% PFA in PBS, then washed 3 × 20 min in PBS. DiI (Invitrogen, 40μM CM-DiI in ethanol) was loaded into cells using micropipettes and +4 nA current injection for 10 min, followed by 10 min without current for equilibration. Samples were then returned to 4% PFA in PBS at 37°C for 24 hrs to allow diffusion through neuronal processes. For ventricular views, SVZ niche and striatum were dissected in whole-mount preparation[59]. For coronal views, brain samples were sliced into 300 μm sections with VT1000S vibratome (Leica). Neuronal processes were traced and analyzed using 3D filament tracer in Imaris software (Bitplane). Dendritic fields were enveloped with 3D hull surface to provide ellipsoid axis length measurements, with "a" designated as the long axis in either ventricular or coronal views. Imaris filament statistics provided dendritic branch point numbers and 3D-Sholl analysis was run to determine filament crossings through concentric spheres centered on soma. Vybrant DiO (Invitrogen, 40 μM) was dissolved in dichloromethane (Sigma).

M1-CNiFER cell imaging and analyses

Excitation and imaging of CNiFER cells expressing Ca^{2+} indicator protein TN-XXL[60] was performed at 920nm with 40x (0.8 NA, Nikon) water-dipping objective on multiphoton microscope (Prairie Technologies). Emission light was directed through filter-cube containing: T505LPXR dichroic beamsplitter, HQ470/40-2p emission filter, and ET535/30-2p emission filter (Chroma Technologies). Regions-of-interest were drawn around individual M1-CNiFER cells with average fluorescence for each time point analyzed using Igor Pro software (Wavemetrics). Fluorescence and FRET ratio changes were analyzed as described previously[36]. For SVZ transplantation experiments, cultured M1-CNiFER cells were triturated from dishes by pipetting without trypsin, re-suspended in

ACSF, followed by injection into acute brain slices with pulled (ID = 40 μm) capillary tube using Picospritzer III (Parker). Donepezil (100 μM) was added to ACSF for acute slice experiments. Light-activation of ChR2EYFP was delivered by TTL control of 473 nm laser (IkeCool).

Optogenetic stimulation and analyses

Placement of cannula under isofluorane anesthesia to target the lateral ventricle was performed as described[61], using implantable mono fiber-optic fiber (200 μm, 0.22 NA, Doric). Protruding ferrule end of cannula was then connected via fiber cord to rotary coupling joint (Doric), allowing free animal movement. Light-stimulation of ChR2EYFP was delivered by TTL control (Master 8, AMPI) of 473 nm laser (IkeCool); protocol = 5 ms pulse duration bursts @ 5 Hz, lasting 10 seconds, given once every 2 minutes as described[40]. Light-inhibition with ArchGFP was performed by TLL-controlled 556 nm laser (IkeCool), on for duration of experiment. For SVZ p-rpS6, Ki67, Mash1, DCX, Nestin, Iba1, CD11b, NG2 analyses, 50 μm brain coronal sections were cut and collected serially on Leica VT1000S vibratome. Position of optical fiber tract entering the lateral ventricle was first verified, and 5 coronal sections surrounding the fiber tract were selected for analyses, comparing P30 littermates with light vs. no-light stimulation.

SDS-PAGE and immunoblotting

Protein extracts were prepared as described[62], and resolved by electrophoresis through SDS-PAGE and transferred onto nitrocellulose membranes. For FACS-sorting of ChAT+ neurons, brain tissues were first dissociated with neural tissue dissociating kit (Miltenyi) according to manufacturer's protocol, followed by sorting on BD FACS DiVa sorter via genetically-labeled tdTomato fluorescence. Antibodies were diluted in PBS containing 0.2% triton-X100 plus 4% non-fat dry milk, followed by overnight incubation at 4°C. Detection was accomplished through secondary antibodies conjugated to horse-radish peroxidase (Superpicture, Invitrogen) and treated with enhanced chemiluminescence (Thermoscientific). Primary antibodies used include: Ank3 (rabbit, 1:1000, V. Bennett); DCX (#4604, 1:600, Cell Signaling), pFGFR1 (#06-1433, 1:2500, Millipore); pEGFR (#2238, 1:800, Cell Signaling), and actin (#ab3280, 1:2000, Abcam). All antibodies used were validated in our previous publications[12,6] or by publications available on vendor website specific to each antibody.

Statistical analysis

No statistical methods were used to pre-determine samples sizes, but they are similar to those reported elsewhere[11,12,6]. IHC staining cell counting from animal experiments was performed blind to the experimental condition, other data collection and analyses were not performed blind to the conditions. Blocking of experimental design was assigned by animal genotype and was not randomized. Data sets were tested for normality with Igor Pro (WaveMetrics) using serial randomness test. Depending on sample size, Student's *t* test (10) or Wilcoxon two-sample test (5) were used for statistical comparisons between two data sets. One-way ANOVA was performed for multivariate comparisons. In vivo optogenetic experiments were performed on sets of three littermates and compared via one-

way ANOVA for correlated samples. Cell recording data was acquired first in control followed by pharmacological conditions, and compared by one-way ANOVA for correlated samples. Throughout, Tukey box-and-whisker plots were generated via http://boxplot.tyerslab.com/ to depict mean (+), median (line), low and high quartiles (boxes), range (whiskers), and outliers (o).

Supplementary Material

Refer to Web version on PubMed Central for supplementary material.

Acknowledgments

References

1. Kelsch W, Sim S, Lois C. Watching synaptogenesis in the adult brain. Annu Rev Neurosci. 2010; 33:131–149. [PubMed: 20572770]

2. Ihrie RA, Alvarez-Buylla A. Lake-front property: a unique germinal niche by the lateral ventricles of the adult brain. Neuron. 2011; 70:674–686. [PubMed: 21609824]

3. Lazarini F, Lledo PM. Is adult neurogenesis essential for olfaction? Trends Neurosci. 2011; 34:20–30. [PubMed: 20980064]

4. Aboody K, Capela A, Niazi N, Stern JH, Temple S. Translating stem cell studies to the clinic for CNS repair: current state of the art and the need for a Rosetta stone. Neuron. 2011; 70:597–613. [PubMed: 21609819]

5. Robel S, Berninger B, Gotz M. The stem cell potential of glia: lessons from reactive gliosis. Nat Rev Neurosci. 2011; 12:88–104. [PubMed: 21248788]

6. Benner EJ, Luciano D, Jo R, Abdi K, Paez-Gonzalez P, Sheng H, Warner DS, Liu C, Eroglu C, Kuo CT. Protective astrogenesis from the SVZ niche after injury is controlled by Notch modulator Thbs4. Nature. 2013; 497:369–373. [PubMed: 23615612]

7. Kriegstein A, Alvarez-Buylla A. The glial nature of embryonic and adult neural stem cells. Annu Rev Neurosci. 2009; 32:149–184. [PubMed: 19555289]

8. Suh H, Deng W, Gage FH. Signaling in adult neurogenesis. Annu Rev Cell Dev Biol. 2009; 25:253–275. [PubMed: 19575663]

9. Shen Q, Goderie SK, Jin L, Karanth N, Sun Y, Abramova N, Vincent P, Pumiglia K, Temple S. Endothelial cells stimulate self-renewal and expand neurogenesis of neural stem cells. Science. 2004; 304:1338–1340. [PubMed: 15060285]

10. Tavazoie M, Van der Veken L, Silva-Vargas V, Louissaint M, Colonna L, Zaidi B, Garcia-Verdugo JM, Doetsch F. A specialized vascular niche for adult neural stem cells. Cell Stem Cell. 2008; 3:279–288. [PubMed: 18786415]

11. Kuo CT, Mirzadeh Z, Soriano-Navarro M, Rasin M, Wang D, Shen J, Sestan N, Garcia-Verdugo J, Alvarez-Buylla A, Jan LY, Jan YN. Postnatal deletion of Numb/Numblike reveals repair and remodeling capacity in the subventricular neurogenic niche. Cell. 2006; 127:1253–1264. [PubMed: 17174898]

12. Paez-Gonzalez P, Abdi K, Luciano D, Liu Y, Soriano-Navarro M, Rawlins E, Bennett V, Garcia-Verdugo J, Kuo CT. Ank3-dependent SVZ niche assembly is required for the continued production of new neurons. Neuron. 2011; 71:61–75. [PubMed: 21745638]

13. Miller FD, Gauthier-Fisher A. Home at last: neural stem cell niches defined. Cell Stem Cell. 2009; 4:507–510. [PubMed: 19497279]

14. Bovetti S, Gribaudo S, Puche AC, De Marchis S, Fasolo A. From progenitors to integrated neurons: role of neurotransmitters in adult olfactory neurogenesis. J Chem Neuroanat. 2011; 42:304–316. [PubMed: 21641990]

15. Young SZ, Taylor MM, Bordey A. Neurotransmitters couple brain activity to subventricular zone neurogenesis. Eur J Neurosci. 2011; 33:1123–1132. [PubMed: 21395856]

16. Brazel CY, Nunez JL, Yang Z, Levison SW. Glutamate enhances survival and proliferation of neural progenitors derived from the subventricular zone. Neurosci. 2005; 131:55–65.

17. Platel JC, Dave KA, Gordon V, Lacar B, Rubio ME, Bordey A. NMDA receptors activated by subventricular zone astrocytic glutamate are critical for neuroblast survival prior to entering a synaptic network. Neuron. 2010; 65:859–872. [PubMed: 20346761]

18. Lin CW, Sim S, Ainsworth A, Okada M, Kelsch W, Lois C. Genetically increased cell-intrinsic excitability enhances neuronal integration into adult brain circuits. Neuron. 2010; 65:32–39. [PubMed: 20152111]

19. Liu X, Wang Q, Haydar TF, Bordey A. Nonsynaptic GABA signaling in postnatal subventricular zone controls proliferation of GFAP-expressing progenitors. Nat Neurosci. 2005; 8:1179–1187. [PubMed: 16116450]

20. Alfonso J, Le Magueresse C, Zuccotti A, Khodosevich K, Monyer H. Diazepam binding inhibitor promotes progenitor proliferation in the postnatal SVZ by reducing GABA signaling. Cell Stem Cell. 2012; 10:76–87. [PubMed: 22226357]

21. Young SZ, Platel JC, Nielsen JV, Jensen NA, Bordey A. GABA(A) Increases Calcium in Subventricular Zone Astrocyte-Like Cells Through L- and T-Type Voltage-Gated Calcium Channels. Front Cell Neurosci. 2010; 4:8. [PubMed: 20422045]

22. Van Kampen JM, Hagg T, Robertson HA. Induction of neurogenesis in the adult rat subventricular zone and neostriatum following dopamine D3 receptor stimulation. Eur J Neurosci. 2004; 19:2377–2387. [PubMed: 15128392]

23. O'Keeffe GC, Tyers P, Aarsland D, Dalley JW, Barker RA, Caldwell MA. Dopamine-induced proliferation of adult neural precursor cells in the mammalian subventricular zone is mediated through EGF. Proc Natl Acad Sci USA. 2009; 106:8754–8759. [PubMed: 19433789]

24. Banasr M, Hery M, Printemps R, Daszuta A. Serotonin-induced increases in adult cell proliferation and neurogenesis are mediated through different and common 5-HT receptor subtypes in the dentate gyrus and the subventricular zone. Neuropsychopharm. 2004; 29:450–460.

25. Tong CK, Chen J, Cebrian-Silla A, Mirzadeh Z, Obernier K, Guinto CD, Tecott LH, Garcia-Verdugo JM, Kriegstein A, Alvarez-Buylla A. Axonal Control of the Adult Neural Stem Cell Niche. Cell Stem Cell. 2014; 14:500–511. [PubMed: 24561083]

26. Cooper-Kuhn CM, Winkler J, Kuhn HG. Decreased neurogenesis after cholinergic forebrain lesion in the adult rat. J Neurosci Res. 2004; 77:155–165. [PubMed: 15211583]

27. Mudo G, Belluardo N, Mauro A, Fuxe K. Acute intermittent nicotine treatment induces fibroblast growth factor-2 in the subventricular zone of the adult rat brain and enhances neuronal precursor cell proliferation. Neurosci. 2007; 145:470–483.

28. Misgeld T, Burgess RW, Lewis RM, Cunningham JM, Lichtman JW, Sanes JR. Roles of neurotransmitter in synapse formation: development of neuromuscular junctions lacking choline acetyltransferase. Neuron. 2002; 36:635–648. [PubMed: 12441053]

29. de Castro BM, De Jaeger X, Martins-Silva C, Lima RD, Amaral E, Menezes C, Lima P, Neves CM, Pires RG, Gould TW, Welch I, Kushmerick C, Guatimosim C, Izquierdo I, Cammarota M, Rylett RJ, Gomez MV, Caron MG, Oppenheim RW, Prado MA, Prado VF. The vesicular acetylcholine transporter is required for neuromuscular development and function. Mol Cell Biol. 2009; 29:5238–5250. [PubMed: 19635813]

30. Zhou D, Lambert S, Malen PL, Carpenter S, Boland LM, Bennett V. AnkyrinG is required for clustering of voltage-gated Na channels at axon initial segments and for normal action potential firing. J Cell Biol. 1998; 143:1295–1304. [PubMed: 9832557]

31. Kordeli E, Lambert S, Bennett V. AnkyrinG. A new ankyrin gene with neural-specific isoforms localized at the axonal initial segment and node of Ranvier. J Biol Chem. 1995; 270:2352–2359. [PubMed: 7836469]

32. Patel JC, Rossignol E, Rice ME, Machold RP. Opposing regulation of dopaminergic activity and exploratory motor behavior by forebrain and brainstem cholinergic circuits. Nat Commun. 2012; 3:1172. [PubMed: 23132022]

33. Guzman MS, De Jaeger X, Raulic S, Souza IA, Li AX, Schmid S, Menon RS, Gainetdinov RR, Caron MG, Bartha R, Prado VF, Prado MA. Elimination of the vesicular acetylcholine transporter in the striatum reveals regulation of behaviour by cholinergic-glutamatergic co-transmission. PLoS Biol. 2011; 9:e1001194. [PubMed: 22087075]

34. Bennett BD, Wilson CJ. Spontaneous activity of neostriatal cholinergic interneurons in vitro. J Neurosci. 1999; 19:5586–5596. [PubMed: 10377365]

35. Ding JB, Guzman JN, Peterson JD, Goldberg JA, Surmeier DJ. Thalamic gating of corticostriatal signaling by cholinergic interneurons. Neuron. 2010; 67:294–307. [PubMed: 20670836]

36. Nguyen QT, Schroeder LF, Mank M, Muller A, Taylor P, Griesbeck O, Kleinfeld D. An in vivo biosensor for neurotransmitter release and in situ receptor activity. Nat Neurosci. 2010; 13:127–132. [PubMed: 20010818]

37. Doetsch F, Garcia-Verdugo JM, Alvarez-Buylla A. Cellular composition and three-dimensional organization of the subventricular germinal zone in the adult mammalian brain. J Neurosci. 1997; 17:5046–5061. [PubMed: 9185542]

38. Bertran-Gonzalez J, Chieng BC, Laurent V, Valjent E, Balleine BW. Striatal cholinergic interneurons display activity-related phosphorylation of ribosomal protein S6. PLoS One. 2012; 7:e53195. [PubMed: 23285266]

39. Knight ZA, Tan K, Birsoy K, Schmidt S, Garrison JL, Wysocki RW, Emiliano A, Ekstrand MI, Friedman JM. Molecular profiling of activated neurons by phosphorylated ribosome capture. Cell. 2012; 151:1126–1137. [PubMed: 23178128]

40. Nagode DA, Tang AH, Karson MA, Klugmann M, Alger BE. Optogenetic release of ACh induces rhythmic bursts of perisomatic IPSCs in hippocampus. PLoS One. 2011; 6:e27691. [PubMed: 22110723]

41. Ma W, Maric D, Li BS, Hu Q, Andreadis JD, Grant GM, Liu QY, Shaffer KM, Chang YH, Zhang L, Pancrazio JJ, Pant HC, Stenger DA, Barker JL. Acetylcholine stimulates cortical precursor cell proliferation in vitro via muscarinic receptor activation and MAP kinase phosphorylation. Eur J Neurosci. 2000; 12:1227–1240. [PubMed: 10762352]

42. Campbell JS, Wenderoth MP, Hauschka SD, Krebs EG. Differential activation of mitogen-activated protein kinase in response to basic fibroblast growth factor in skeletal muscle cells. Proc Natl Acad Sci USA. 1995; 92:870–874. [PubMed: 7846069]

43. Shingo T, Gregg C, Enwere E, Fujikawa H, Hassam R, Geary C, Cross JC, Weiss S. Pregnancy-stimulated neurogenesis in the adult female forebrain mediated by prolactin. Science. 2003; 299:117–120. [PubMed: 12511652]

44. Wang W, Pan YW, Wietecha T, Zou J, Abel GM, Kuo CT, Xia Z. Extracellular signal-regulated kinase 5 (ERK5) mediates prolactin-stimulated adult neurogenesis in the subventricular zone and olfactory bulb. J Biol Chem. 2013; 288:2623–2631. [PubMed: 23223235]

45. Mak GK, Enwere EK, Gregg C, Pakarainen T, Poutanen M, Huhtaniemi I, Weiss S. Male pheromone-stimulated neurogenesis in the adult female brain: possible role in mating behavior. Nat Neurosci. 2007; 10:1003–1011. [PubMed: 17603480]

46. Mak GK, Weiss S. Paternal recognition of adult offspring mediated by newly generated CNS neurons. Nat Neurosci. 2010; 13:753–758. [PubMed: 20453850]

47. Markwardt SJ, Dieni CV, Wadiche JI, Overstreet-Wadiche L. Ivy/neurogliaform interneurons coordinate activity in the neurogenic niche. Nat Neurosci. 2011; 14:1407–1409. [PubMed: 21983681]

48. Song J, Zhong C, Bonaguidi MA, Sun GJ, Hsu D, Gu Y, Meletis K, Huang ZJ, Ge S, Enikolopov G, Deisseroth K, Luscher B, Christian KM, Ming GL, Song H. Neuronal circuitry mechanism regulating adult quiescent neural stem-cell fate decision. Nature. 2012; 489:150–154. [PubMed: 22842902]

Author Manuscript Author Manuscript Author Manuscript Author Manuscript

49. Song J, Sun J, Moss J, Wen Z, Sun GJ, Hsu D, Zhong C, Davoudi H, Christian KM, Toni N, Ming GL, Song H. Parvalbumin interneurons mediate neuronal circuitry-neurogenesis coupling in the adult hippocampus. Nat Neurosci. 2013; 16:1728–1730. [PubMed: 24212671]

50. Young SZ, Taylor MM, Wu S, Ikeda-Matsuo Y, Kubera C, Bordey A. NKCC1 Knockdown Decreases Neuron Production through GABAA-Regulated Neural Progenitor Proliferation and Delays Dendrite Development. J Neurosci. 2012; 32:13630–13638. [PubMed: 23015452]

51. Gong S, Doughty M, Harbaugh CR, Cummins A, Hatten ME, Heintz N, Gerfen CR. Targeting Cre recombinase to specific neuron populations with bacterial artificial chromosome constructs. J Neurosci. 2007; 27:9817–9823. [PubMed: 17855595]

52. Gong S, Zheng C, Doughty ML, Losos K, Didkovsky N, Schambra UB, Nowak NJ, Joyner A, Leblanc G, Hatten ME, Heintz N. A gene expression atlas of the central nervous system based on bacterial artificial chromosomes. Nature. 2003; 425:917–925. [PubMed: 14586460]

53. Jenkins PM, Vasavda C, Hostettler J, Davis JQ, Abdi K, Bennett V. E-cadherin Polarity Is Determined by a Multifunction Motif Mediating Lateral Membrane Retention through Ankyrin-G and Apical-lateral Transcytosis through Clathrin. J Biol Chem. 2013; 288:14018–14031. [PubMed: 23530049]

54. Scheffler B, Walton NM, Lin DD, Goetz AK, Enikolopov G, Roper SN, Steindler DA. Phenotypic and functional characterization of adult brain neuropoiesis. Proc Natl Acad Sci USA. 2005; 102:9353–9358. [PubMed: 15961540]

55. Sheikh F, Fandrich RR, Kardami E, Cattini PA. Overexpression of long or short FGFR-1 results in FGF-2-mediated proliferation in neonatal cardiac myocyte cultures. Cardiovasc Res. 1999; 42:696–705. [PubMed: 10533610]

56. Lim DA, Huang YC, Swigut T, Mirick AL, Garcia-Verdugo JM, Wysocka J, Ernst P, Alvarez-Buylla A. Chromatin remodelling factor Mll1 is essential for neurogenesis from postnatal neural stem cells. Nature. 2009; 458:529–533. [PubMed: 19212323]

57. Mirzadeh Z, Merkle FT, Soriano-Navarro M, Garcia-Verdugo JM, Alvarez-Buylla A. Neural stem cells confer unique pinwheel architecture to the ventricular surface in neurogenic regions of the adult brain. Cell Stem Cell. 2008; 3:265–278. [PubMed: 18786414]

58. Kao YH, Sterling P. Matching neural morphology to molecular expression: single cell injection following immunostaining. J Neurocytol. 2003; 32:245–251. [PubMed: 14724387]

59. Mirzadeh Z, Doetsch F, Sawamoto K, Wichterle H, Alvarez-Buylla A. The subventricular zone en-face: wholemount staining and ependymal flow. J Vis Exp. 2010; 39:1938. [PubMed: 20461052]

60. Mank M, Santos AF, Direnberger S, Mrsic-Flogel TD, Hofer SB, Stein V, Hendel T, Reiff DF, Levelt C, Borst A, Bonhoeffer T, Hubener M, Griesbeck O. A genetically encoded calcium indicator for chronic in vivo two-photon imaging. Nat Methods. 2008; 5:805–811. [PubMed: 19160515]

61. Beaulieu JM, Marion S, Rodriguiz RM, Medvedev IO, Sotnikova TD, Ghisi V, Wetsel WC, Lefkowitz RJ, Gainetdinov RR, Caron MG. A beta-arrestin 2 signaling complex mediates lithium action on behavior. Cell. 2008; 132:125–136. [PubMed: 18191226]

62. Abdi KM, Bennett V. Adducin promotes micrometer-scale organization of beta2-spectrin in lateral membranes of bronchial epithelial cells. Mol Biol Cell. 2008; 19:536–545. [PubMed: 18003973]
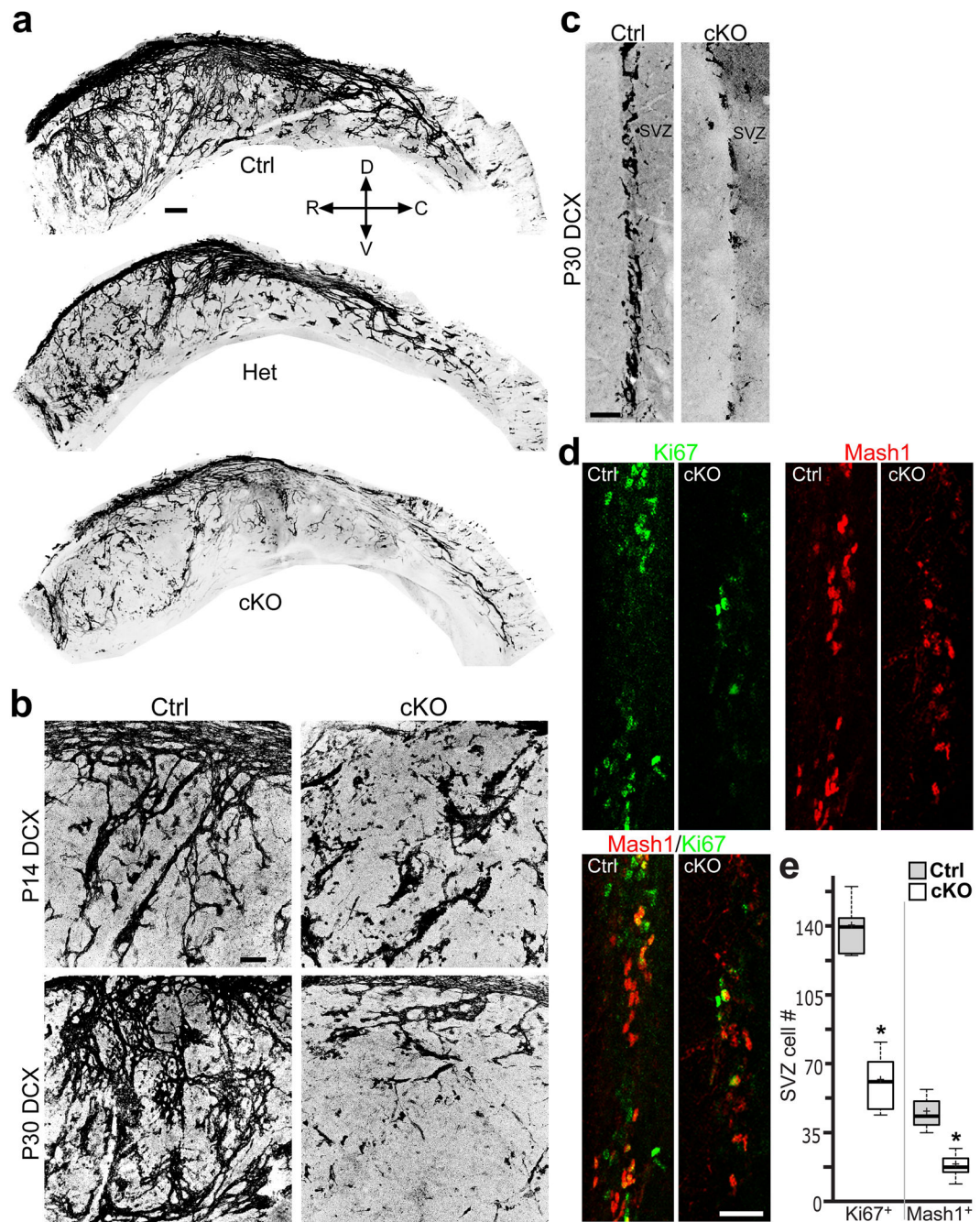
Figure 1. Ank3 deletion in ChAT$^+$ neurons results in postnatal SVZ neurogenesis defects
(**a**) Representative whole-mount DCX staining of SVZ neuroblast chains, showing neurogenesis defects in P30 Ank3-cKO mutant mice. DCX fluorescence signal inverted to black on white for clarity. R = rostral, C = caudal, D = dorsal, V = ventral, Ctrl = control. (**b,c**) Close-up views of SVZ DCX neuroblast defects in P14 and P30 whole-mount preparation (**b**) or P30 coronal sections (**c**) from Ctrl and Ank3-cKO mice. (**d**) Representative IHC staining of Ki67 and Mash1 expression in P30 SVZ niche showing decreased Ki67$^+$ and Mash1$^+$ cell numbers in Ank3-cKO mice. (**e**) Quantifications of SVZ

Ki67, Mash1 IHC staining data from P30 Ctrl and Ank3-cKO animals. * $P < 0.008$, Wilcoxon two-sample test, $n = 5$, $z = 2.611$. Box plots show mean (+), median (−), quartiles (boxes), range (whiskers). Scale bars: 100 μm (**a**), 50 μm (**b,c,d**).
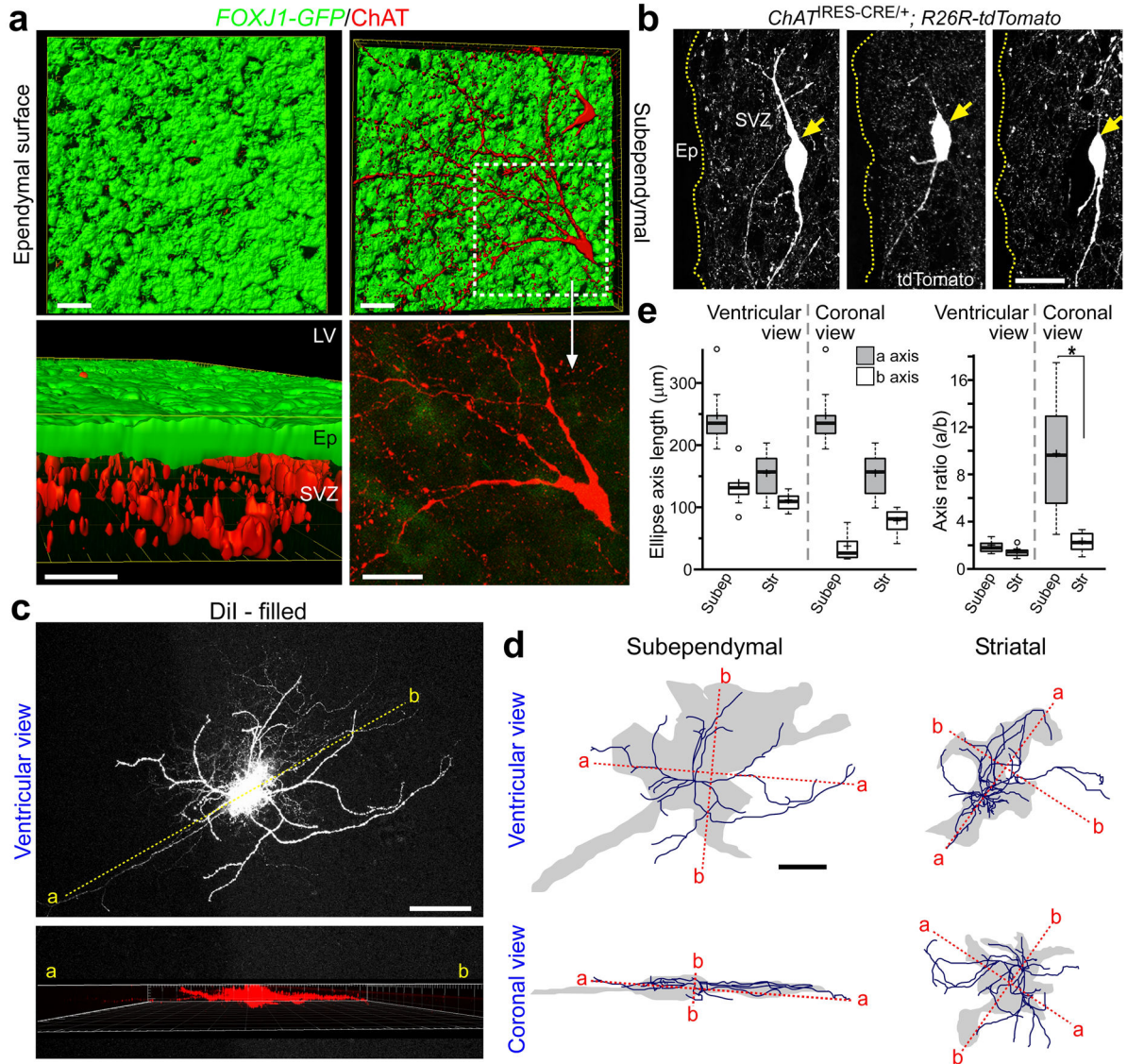
**Figure 2. Identification of subependymal ChAT⁺ neurons**

(**a**) Imaris 3D-projections of IHC staining from SVZ niche whole-mount from P30 *FOXJ1-GFP* animal. Red: ChAT⁺ processes; green: ependymal cells (Ep) visualized by *FOXJ1-GFP* transgene. Note that the ChAT⁺ processes are subependymal. Dashed-box indicates neuronal cell body. LV = lateral ventricle. (**b**) P30 SVZ niche coronal sections from *ChAT*^IRES-Cre/+*; R26R-tdTomato* animals stained with tdTomato antibody. Note the presence of ChAT⁺ neurons (arrows) beneath ependymal cells (Ep, dashed-lines). (**c**) Representative DiI-filling of subep-ChAT⁺ neuron. (Top) En-face ventricular view shows dendritic and axonal processes. (Bottom) Side view of above neuron in 3D reconstruction demonstrates planar arrangement paralleling ependymal surface above (a–b dashed line indicates orientation of side view). (**d**) Traces from ventricular and coronal section views of representative DiI-filled ChAT⁺ neurons. Note the planer vs. non-planar morphologies of subependymal vs. striatal ChAT⁺ neurons in coronal view. Blue lines indicate dendrites, and

grey areas represent axonal fields. (**e**) Quantifications of neuronal morphology from ventricular and coronal views for subependymal (Subep) and striatal (Str) ChAT$^+$ neurons. Traced neurons were fit with an ellipse, and ellipse axis lengths are measured as the long (a) and short axis (b), followed by calculations of axis ratio (a/b). Note the significantly increased axis ratio for subep-ChAT$^+$ neurons in coronal view. * $P < 0.002$, $t_{18} = 4.469$ unpaired Student's t test, $n = 10$. Box plots show mean, median, quartiles, range. Scale bars: 30 μm (**a**), 20 μm (**b**), 50 μm (**c, d**).
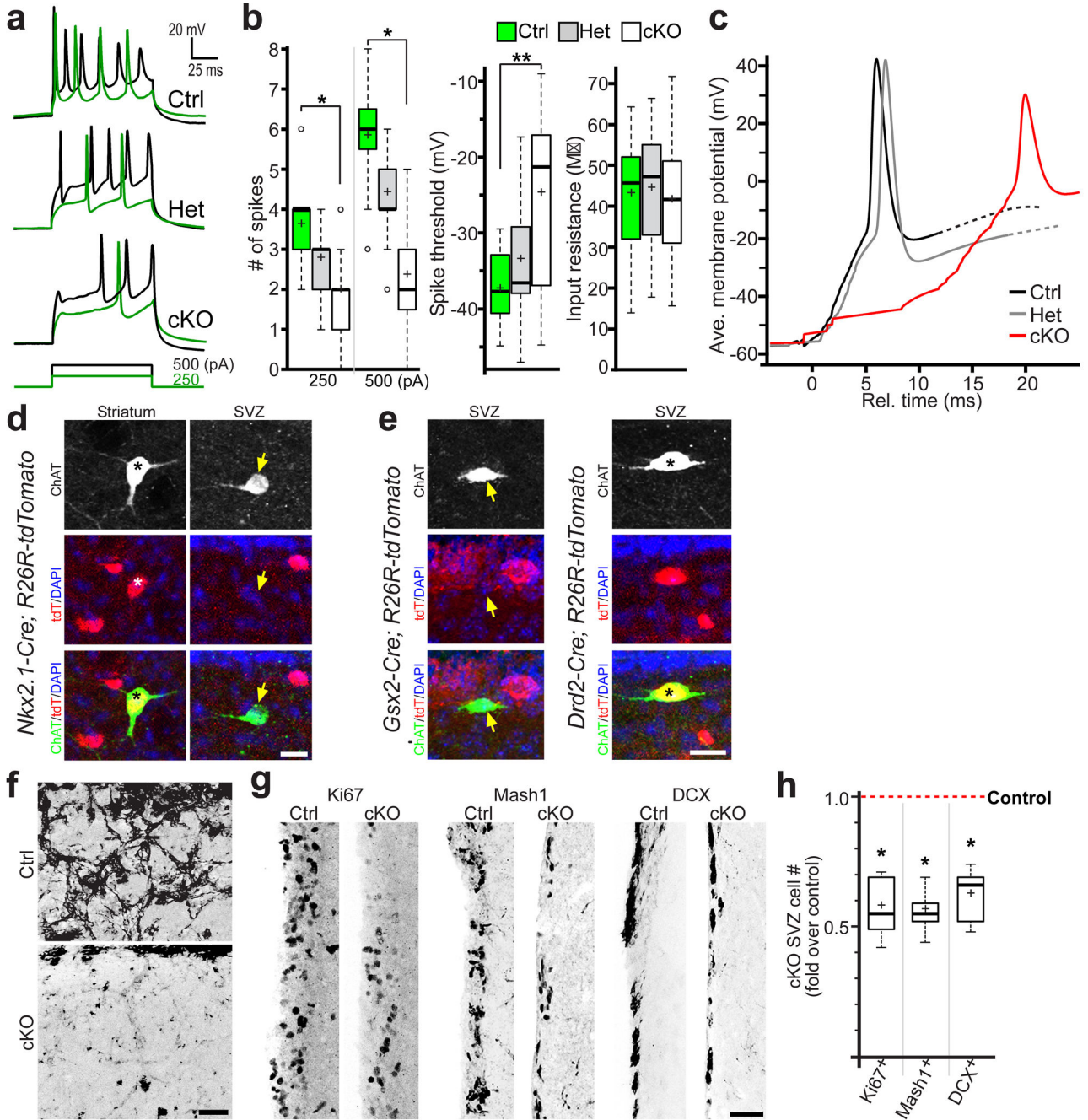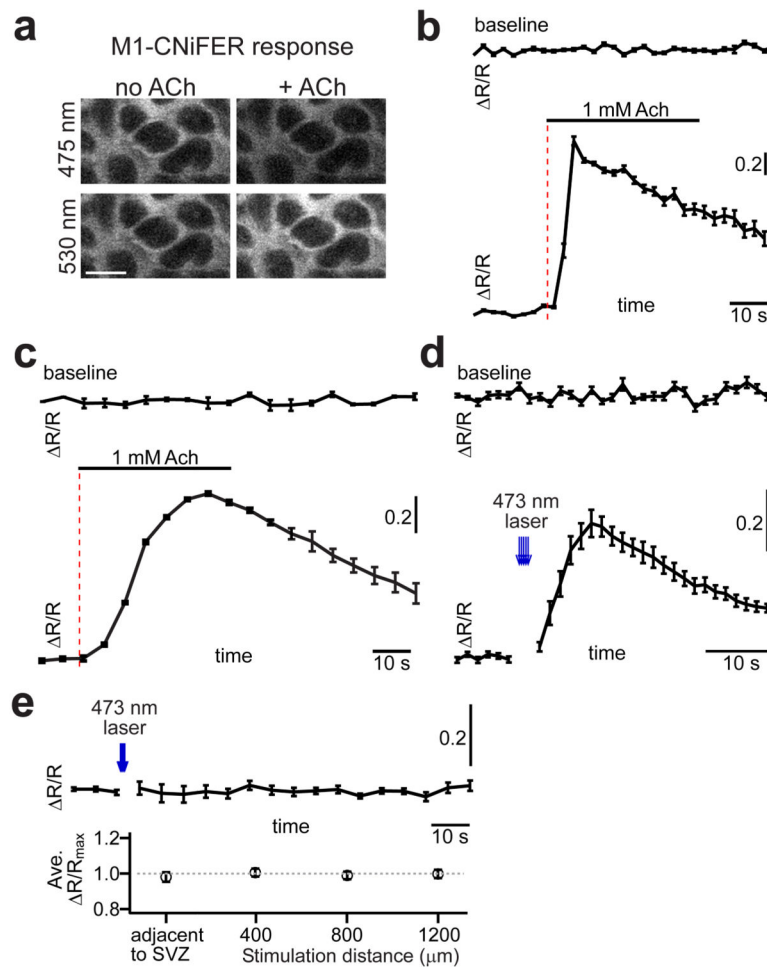
Figure 3.
Defects in subependymal ChAT$^+$ neuron action potential generation and SVZ neurogenesis.
(**a**) Representative current-clamp recordings from subep-ChAT$^+$ neurons in response to 100 ms current pulses (250 pA = green; 500 pA = black trace) in Ank3 Ctrl (top), Het (center), and cKO (bottom) animals. Square trace = duration of current pulse. (**b**) Quantifications of spike numbers to 100 ms current pulses at 250 or 500 pA; spike threshold; and input resistance in subep-ChAT$^+$ neurons from Ctrl, Het, and cKO animals. * $P < 0.0001$, $t_{34} =$ 4.283 (250 pA), $t_{34} = 7.532$ (500 pA), ** $P < 0.0006$, $t_{34} = 3.281$, unpaired Student's t test, n

= 18 in all groups (6 animals). Box plots show mean, median, quartiles, range. (**c**) Mean action potential traces from Ank3 Ctrl, Het, and cKO subep-ChAT$^+$ neurons to 500 pA current injections, showing delayed spiking in cKO neurons. (**d**) ChAT and tdTomato IHC staining on coronal sections from P30 *Nkx2.1-Cre; R26R-tdTomato* mice, showing co-localization in striatal (*) but not subep-ChAT$^+$ (arrows) neurons. (**e**) ChAT and tdTomato IHC staining in subep-ChAT$^+$ neurons from P30 *Gsx2-Cre; R26R-tdTomato* or *Drd2-Cre; R26R-tdTomato* mice, showing co-localization with *Drd2-Cre driver* (arrows). (**f**) Representative views of ventricular whole-mount DCX staining from P30 *Drd2-Cre; ChAT*$^{flox/+}$ (Ctrl) and *Drd2-Cre; ChAT*$^{flox/flox}$ (cKO) mice. (**g**) Representative Ki67, Mash1, DCX IHC staining of SVZ niche from P30 *Drd2-Cre; ChAT*$^{flox/+}$ (Ctrl) and *Drd2-Cre; ChAT*$^{flox/flox}$ (cKO) mice. Fluorescence signals inverted to black on white for clarity. (**h**) Quantifications of SVZ Ki67$^+$, Mash1$^+$, DCX$^+$ IHC staining data from (**g**). * $P < 0.008$, $z = 2.611$, Wilcoxon two-sample test, $n = 5$. Box plots show mean, median, quartiles, range. Scale bars: 15 μm (**d**,**e**), 50 μm (**f**,**g**).
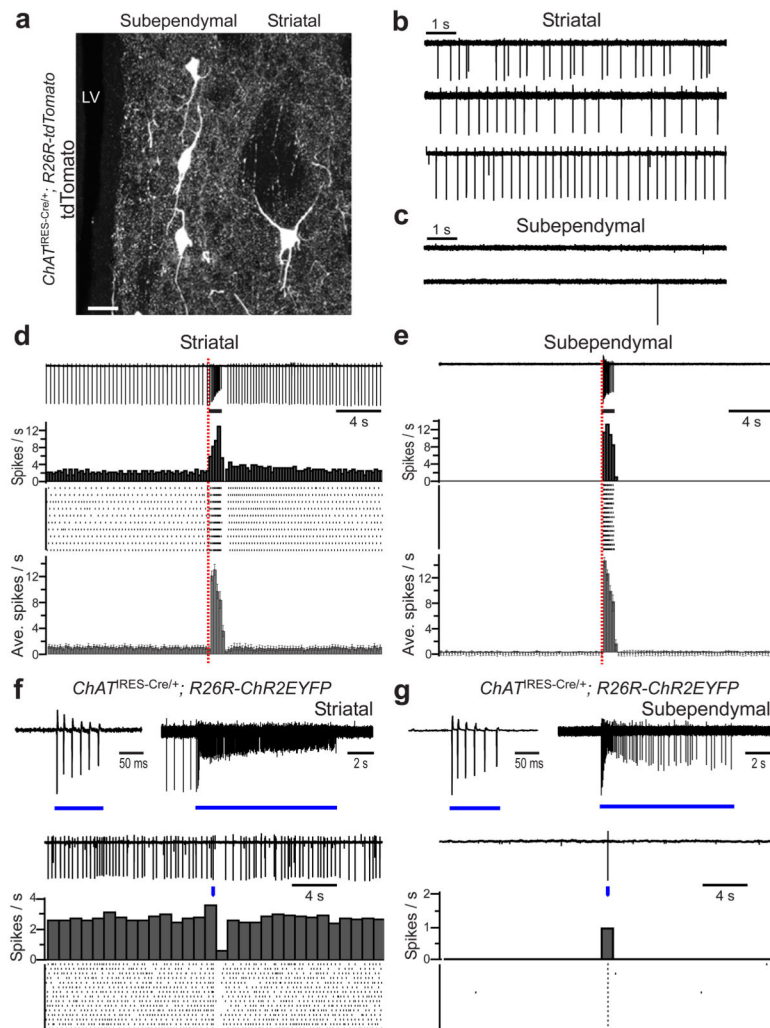
Figure 4. Electrophysiological properties of subependymal ChAT+ neurons
(**a**) tdTomato IHC antibody staining of P30 brain coronal section from *ChAT*[IRES-Cre/+];
R26R-tdTomato animals, showing spatial relationships between subependymal (subep-) and
striatal ChAT+ neurons. (**b**,**c**) Representative traces of cell attached recordings from striatal
(**b**) or subep- (**c**) ChAT+ neurons. (**d**,**e**) Representative traces of cell-attached recordings
from striatal (**d**) and subependymal (**e**) ChAT+ neurons in response to 1 second (s) local
application of 100 μM glutamate. Bar indicates duration of puffed drug. Peristimulus-time
histogram and raster plots for 15 consecutive sweeps, as well as corresponding average
spikes per second (mean ± s.e.m.) are shown below, demonstrating baseline spontaneous
and glutamate-evoked frequencies. Note the robust spike frequency of subep-ChAT+ neuron
during stimulation. Red dashed-lines indicate start of drug application across trials. (**f**,**g**)
Responses of striatal (**f**) or subependymal (**g**) ChAT+ neurons, expressing ChR2EYFP, to
100 ms (top left panel), 10 s (top right panel), or 10 ms (bottom panels) pulses of 473 nm
light. Blue bars indicate duration of light-pulse. For 10 ms light pulses, peristimulus-time
histogram and raster plots for 15 consecutive sweeps are shown below representative traces.
Scale bar: 20 μm (**a**).

Figure 5. Detecting activity-dependent release of ACh in the SVZ niche

(**a**) Representative changes in M1-CNiFER fluorescent responses at 475 and 530 nm emission wavelengths, with and without ACh application. Excitation source: 920 nm laser. (**b–e**) Average traces of M1-CNiFER cell baseline FRET ratios, and ACh- or light-induced changes in FRET ratios (ΔR/R). (**b**) ACh applied to adherent M1-CNiFER cells in culture. Images sampled once every 2.6 seconds. $n = 10$. Mean ± s.e.m. (**c**) ACh applied to M1-CNiFER cells transplanted into SVZ in acute brain slice preparation. Images sampled once every 5.4 seconds. $n = 16$. Mean ± s.e.m. (**d**) M1-CNiFER cells transplanted into SVZ niche in acute slice preparation from $ChAT^{IRES-Cre/+}$; $R26R-ChR2EYFP$ mice, followed by 473 nm light-stimulation to activate subep-ChAT^{+} neurons (5×250 ms light pulses, 2 Hz). Images sampled once every 1.6 seconds. $n = 14$. Mean ± s.e.m. (**e**) Same focal light-stimulation protocol and slice preparation to image SVZ transplanted M1-CNiFER cells as in (**d**), but activating striatal ChAT^{+} neurons adjacent to the SVZ (top trace). Activating striatal ChAT[+] neuron at various distances from SVZ: averages of maximum ΔR/R from multiple slice imaging experiments. $n = 15$. Mean ± s.e.m. Scale bar: 10 μm (**a**).
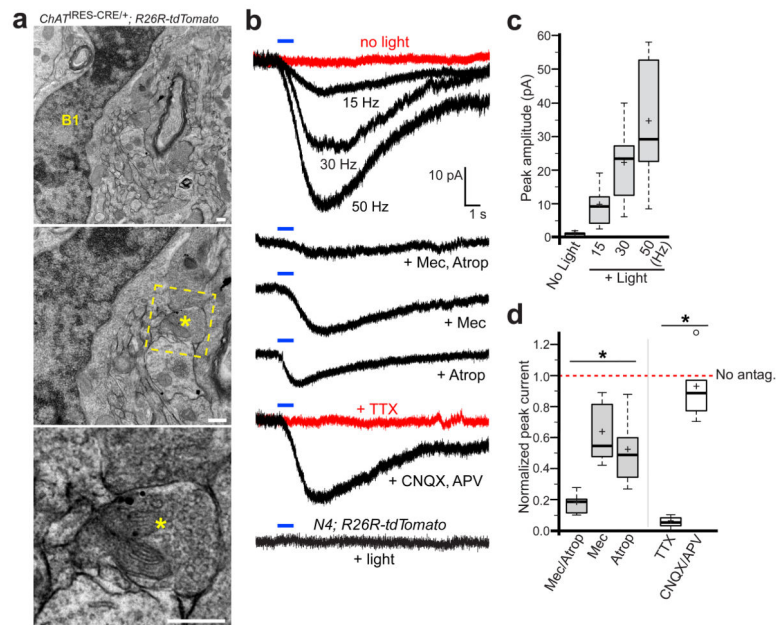
Figure 6. SVZ NSCs respond directly to local ACh release
(**a**) TEM analysis of P30 immunogold-labeled (indicated by black dots) ChAT$^+$ neuronal terminals within SVZ niche. Close-up view showing synaptic vesicles in axon from ChAT$^+$ neuron adjacent to SVZ B-type astrocytic stem cells (B1). * Axon containing synaptic vesicles. (**b**) Representative voltage-clamp recordings from tdTomato$^+$ SVZ NSCs showing: evoked inward currents following 10 ms 473 nm light pulses @ 15, 30, or 50 Hz for 1 second (top traces, red trace is baseline without light). Optogenetically-stimulated currents are sensitive to cholinergic blockers mecamylamine (Mec., 40 μM), atropine (Atrop., 5 μM), are unaffected by glutamatergic blockers CNQX (10 μM) + APV (100 μM) (black trace), but are abolished by blockade of action potentials (TTX 2 μM, red trace). No light-evoked response was found in tdTomato$^+$ SVZ NSCs using identical experimental conditions from P30 *nestin-CreER$^{tm}4$; R26R-tdTomato* mice (without *ChAT-ChR2EYFP*). Blue bar = duration of light-stimulation train (10 ms pulses, 30 Hz unless otherwise noted). (**c**) Quantifications of current responses to different light-stimulation frequencies shown in (**b**), $n = 8$. Box plots show mean, median, quartiles, range. (**d**) Quantifications of light-evoked current responses under pharmacological conditions shown in (**b**). * $P < 0.0006$, $F_{3,21} = 8.81$ (Mec/Atrop), $F_{2,13} = 14.02$ (TTX), one-way ANOVA, $n ≥ 5$ in all groups. Box plots show mean, median, quartiles, range. Scale bar: 250 nm (**a**).
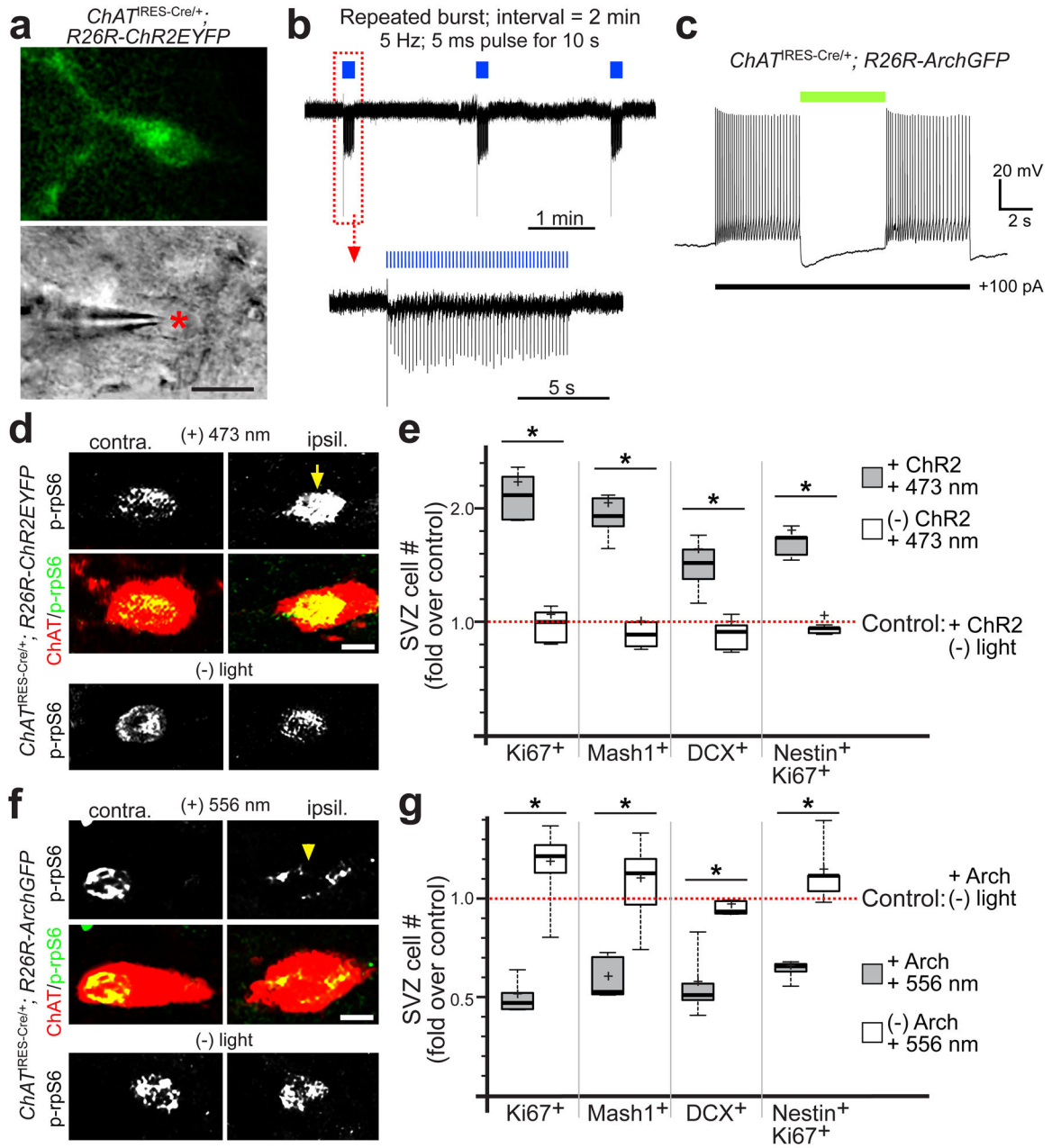
Figure 7. Optogenetic modulation of SVZ niche cellular proliferation and neurogenesis
(**a**) Images of ChR2EYFP-expressing subep-ChAT[+] neuron (*) and cell-attached configuration. (**b**) Representative trace of cell-attached recordings from subep-ChAT^{+} neurons from P30 *ChAT*[IRES-Cre/+]*; R26R-ChR2EYFP* mice, responding to pulses of 473 nm light-stimulation. Blue bars indicate duration of light-induction. (**c**) Optogenetic silencing of subep-ChAT^{+} neurons during whole-cell recording from *ChAT*[IRES-Cre/+]*; R26R-ArchGFP* mice. Neuronal spiking was induced via 15 second, 100 pA depolarizing current (indicated by lower bar). 5 second pulse of 556 nm light (green bar) abolished spiking. (**d**) Representative p-rpS6 IHC staining of subep-ChAT^{+} neurons following 48 hrs of 473 nm light-stimulation, comparing induced ipsilateral (ipsil.) to uninduced contralateral (contra.)

SVZ, imaged at identical settings from same section. Note the increase in p-rpS6 expression in subep-ChAT$^+$ neuron in light-induced condition (arrow). (**e**) Quantifications of SVZ Ki67$^+$, Mash1$^+$, DCX$^+$, and Nestin$^+$Ki67$^+$ IHC staining data from *ChAT*$^{IRES-Cre/+}$*; R26R-ChR2EYFP* littermates without light-stimulation (control; + ChR2, − light); with light-stimulation (+ ChR2, + 473 nm); and from *R26R-ChR2EYFP* (no *ChAT*$^{IRES-Cre/+}$) littermate with light-stimulation (− ChR2, + 473 nm). * $P < 0.003$, $F_{2,15} = 26.08$ (Ki67), $F_{2,15} = 8.91$ (Mash1), $F_{2,12} = 14.11$ (DCX), $F_{2,12} = 173.7$ (Nestin/Ki67), one-way ANOVA, n 5 in all groups. Box plots show mean, median, quartiles, range. (**f**) Representative p-rpS6 IHC staining of subep-ChAT$^+$ neurons following 48 hrs of 556 nm light-stimulation, comparing induced ipsilateral to uninduced contralateral SVZ, imaged at identical settings from same section. Note the decrease in p-rpS6 expression in subep-ChAT$^+$ neuron in light-induced condition (arrowhead). Cy5 channel used for p-rpS6 secondary antibody staining, for clarity represented in green channel for co-localization with tdTomato. (**g**) Quantifications of SVZ Ki67$^+$, Mash1$^+$, DCX$^+$, and Nestin$^+$Ki67$^+$ IHC staining data from *ChAT*$^{IRES-Cre/+}$*; R26R-ArchGFP* littermates without light-stimulation (control; + Arch, − light); with light-stimulation (+ Arch, + 556 nm); and from *R26R-ArchGFP* (no *ChAT*$^{IRES-Cre/+}$) littermate with light-stimulation (− Arch, + 556 nm). * $P < 0.005$, $F_{2,15} = 16.85$ (Ki67), $F_{2,15} = 13.21$ (Mash1), $F_{2,12} = 26.3$ (DCX), $F_{2,12} = 28.28$ (Nestin/Ki67), one-way ANOVA, n 5 in all groups. Box plots show mean, median, quartiles, range. Scale bar: 10 μm (**a**), 5 μm (**d,f**).